

An Efficient Parameterization for Surface 3D Radiative Effects in Large-Eddy Simulations

Mirjam Tijhuis¹, Bart J. H. van Stratum¹, and Chiel C. van Heerwaarden¹

¹Meteorology and Air Quality Group, Wageningen University and Research, Wageningen, the Netherlands

Key Points:

- We correct simulations with 1D radiation for the 3D radiative effects in a post-processing step with negligible computational overhead
- The probability distributions of diffuse and global radiation closely match the observations after filtering the surface diffuse radiation
- The filter size can be parameterized as a linear function of the cloud cover

Corresponding author: Mirjam Tijhuis, mirjam.tijhuis@wur.nl

Abstract

Most atmospheric models consider radiative transfer only in the vertical direction (1D), as 3D radiative transfer calculations are too costly. Thereby, horizontal transfer of radiation is omitted, resulting in incorrect surface radiation fields. The horizontal spreading of diffuse radiation results in darker cloud shadows, whereas it increases the surface radiation in clear sky patches (cloud enhancement). In this study, we developed a simple method to account for the horizontal transfer of diffuse radiation. We spatially filter the surface diffuse radiation field with a Gaussian filter, which is conceptually simple and computationally efficient. We applied the filtering to the results of Large-Eddy Simulations for two summer days in Cabauw, the Netherlands, on which shallow cumulus clouds formed during the day. We obtained the optimal filter size by matching the simulation results with detailed high-quality observations (1Hz). Without the filtering, cloud enhancements are not captured, and the probability distribution of global radiation is unimodal, whereas the observed distribution is bimodal. After filtering, the probability distribution of global radiation is bimodal and cloud enhancements are simulated, in line with the observations. We found that small changes in the filter width do not strongly influence the results. Furthermore, we showed that the width of the filter can be parameterized as a linear function of e.g. the cloud cover. Hence, this work presents a proof-of-concept for our method to come to more realistic surface irradiances by filtering diffuse radiation at the surface.

Plain Language Summary

The pattern of radiation at the surface is characterized by the presence of cloud shadows and peaks in the radiation caused by scattering of light by clouds. The amount of solar radiation that reaches the Earth's surface determines how much energy is produced by solar panels and how much heat and moisture is supplied to the clouds, thus it influences how the clouds develop. Existing models neglect the scattering of radiation in the horizontal direction, therefore the high peaks in the radiation are not modelled. In this paper, we show how we can include the effect of the horizontal propagation of radiation. We redistribute the radiation at the surface, and we compare our model results with measurements. After the redistribution, the high peaks in radiation are modelled. In general, we get a good match between the observed and modelled radiation distribution. We show that the redistribution can be made a function of the clouds in the model. Hence, this work presents a proof-of-concept for our method to come to more realistic surface radiation, without complex calculations.

1 Introduction

The amount of solar energy that reaches the earth surface is strongly influenced by the complex interactions between clouds and radiation. Therefore, solar energy partly reaches the surface directly and partly reaches the surface as diffuse radiation after it is scattered in the atmosphere by gasses, aerosols and clouds. The total amount of solar energy reaching the surface, also referred to as surface irradiance or global radiation, governs many processes at the surface. It drives the sensible and latent heat fluxes, which supply moisture and energy to boundary layer clouds and thus determine their development. Apart from the surface fluxes, the surface irradiance also influences plant photosynthesis, as diffuse radiation is taken up by the canopy more efficiently than direct radiation (Kanniah et al., 2012). Furthermore, surface irradiance determines the production of renewable energy by solar panels. It is therefore important to have a good model representation of the surface irradiance and the partitioning between direct and diffuse radiation.

Currently, clouds as well as radiation are usually parameterized in weather and climate models. Existing parameterizations for radiation generally neglect the horizontal

61 transport of radiation. Recent methods (Schäfer et al., 2016; Hogan et al., 2016) can ac-
62 count for the horizontal transport of radiation through cloud sides within grid boxes, mak-
63 ing it possible to include the mean 3D effects in general circulation models. Between grid
64 boxes, the horizontal transport can only be neglected if the grid boxes are large enough
65 such that a cloud and its shadow fall within the same grid cell (Wapler & Mayer, 2008).
66 As computing capacity increases, so does the model resolution. With that it becomes
67 possible to resolve individual clouds and horizontal transport of radiation between grid
68 boxes is no longer negligible (Wissmeier et al., 2013). Thus, it becomes increasingly rel-
69 evant to improve existing parameterizations to account for the horizontal transport of
70 radiation in a computationally efficient way.

71 In Large-Eddy Simulations (LES), clouds are resolved explicitly, but the calcula-
72 tion of radiative transfer is still simplified. It is common to consider radiative transfer
73 in 1D and within separate vertical columns (Independent Column Approximation, ICA),
74 to keep calculations affordable. Calculating radiative transfer in 1D omits the horizon-
75 tal transfer of radiation, resulting in incorrect surface radiation fields. There are two main
76 problems. Firstly, in 1D, the cloud shadow is located exactly below the cloud. In real-
77 ity, the cloud shadow is displaced and elongated. The displacement of the cloud shadow
78 can impact the cloud size (Veerman et al., 2020), trigger secondary circulations (Gronemeier
79 et al., 2017) and increase the formation of cloud streets (Jakub & Mayer, 2017). Secondly,
80 the diffuse radiation reaches the surface exactly under the cloud in 1D. In reality, dif-
81 fuse radiation is spread out over a larger surface area (Wissmeier et al., 2013; Wapler
82 & Mayer, 2008; Hogan & Shonk, 2013). The horizontal spreading of the diffuse radia-
83 tion results in darker cloud shadows, whereas it increases the surface radiation in clear
84 sky patches (cloud enhancement). This spreading causes the characteristic bimodal dis-
85 tribution of solar irradiance observed under cloudy conditions (Schmidt et al., 2007, 2009;
86 Gristey et al., 2020; Kreuwel et al., 2020). Gristey et al. (2020) showed that there is a
87 clear difference in the probability distribution of global radiation between on one hand
88 simulations with 1D radiative transfer and on the other hand observations and simula-
89 tions with 3D radiative transfer. This difference is caused by the lack of horizontal spread-
90 ing of diffuse radiation. Therefore, the spreading of the diffuse radiation is the focus point
91 of this study.

92 Different methods exist to include 3D radiative effects or account for them. Ra-
93 diative transfer can be computed accurately in 3D, for example with a Monte Carlo sim-
94 ulation (Mayer, 2009), but these calculations are orders of magnitude slower than 1D cal-
95 culations. A more efficient 3D method is the TenStream solver (Jakub & Mayer, 2015).
96 However, the TenStream solver is not diffusive enough and still more than an order of
97 magnitude slower than 1D calculations (Veerman et al., 2020; Jakub & Mayer, 2015).
98 Alternatively, 1D radiative transfer calculations can be adapted to account for the 3D
99 radiative effects in a computationally efficient way. The errors in the location and shape
100 of the cloud shadow can be tackled by using tilted columns (Tilted Independent Column
101 Approximation, TICA) (e.g., Wissmeier et al., 2013; Wapler & Mayer, 2008; Várnai &
102 Davies, 1999). The spreading of the diffuse radiation can be included by smoothing the
103 1D diffuse radiation fields (Nonlocal Independent Column Approximation, NICA, Marshak
104 et al. (1995)). Especially these smoothing methods strongly simplify the actual radia-
105 tive transfer. It is therefore very important to thoroughly validate the performance of
106 these methods. In previous work, the smoothing was based on and validated against 3D
107 simulations (Marshak et al., 1995; Zuidema & Evans, 1998; Wapler & Mayer, 2008; Wiss-
108 meier et al., 2013). As these 3D simulations are expensive, the validation was limited
109 to snapshots of cloud fields. Instead, we will use observation for the development and
110 validation of our smoothing method, which allows us to test our method over a period
111 of time. Different options exist to smooth the diffuse radiation. The simplest option is
112 to use the area average diffuse radiation for the whole study area (Wapler & Mayer, 2008),
113 which works well for small domains sizes with a regular cloud field, but often a more gen-
114 erally applicable approach, such as a smoothing filter, is required. Possible filters use a

115 gamma distribution (Marshak et al., 1995) or a Gaussian distribution (Zuidema & Evans,
 116 1998; Wissmeier et al., 2013). The simplest distribution, the Gaussian, requires the de-
 117 termination of only one parameter, the standard deviation (σ). σ can be pa-
 118 rameterized for use in operational models. Wissmeier et al. (2013) proposed a method
 119 where σ is a function of the solar zenith angle and the distance from the center of
 120 the surface pixel to the center of the base of the closest cloud. This method requires the
 121 calculation of many σ s, as σ differs per surface pixel.

122 The main aim of this study is to investigate the performance of a simple, compu-
 123 tationally efficient method to account for the horizontal spreading of diffuse radiation
 124 at the surface. We will use a spatial filter to smooth the diffuse radiation at the surface,
 125 similar to Wissmeier et al. (2013), but we use observations to determine how the diffuse
 126 radiation from an LES with 1D radiative transfer can be smoothed best. The observa-
 127 tions are from the Baseline Surface Radiation Network (BSRN) site in Cabauw, the Nether-
 128 lands, and have a 1 second resolution. We can determine how the filtering of the diffuse
 129 radiation should change over time as the cloud field changes, as we do not rely on ex-
 130 pensive 3D calculations to compare to our 1D simulations. Additionally, the advantage
 131 of observations is that they are measurements of reality and not influenced by any model
 132 parameterization or assumption. We aim to keep the parameterization as simple as pos-
 133 sible, thus we will use one filter size per time step for the whole domain.

134 2 Data

135 For this study, we selected two summer days (4 July and 15 August 2016) in Cabauw,
 136 the Netherlands, during which shallow cumulus clouds formed. The 3D radiative effects
 137 are most pronounced when cloud shadows and regions with cloud enhancements both
 138 occur frequently, thus we selected days with highly variable surface global radiation. Fur-
 139 thermore, ice and liquid water impact radiation differently, thus we selected days with-
 140 out high clouds (which contain ice). Lastly, we are interested in clouds that are surface
 141 driven, as the formation of these clouds is the result of the local surface irradiance. There-
 142 fore, we selected days that started and ended with cloud-free skies and had shallow cu-
 143 mulus clouds during the day.

144 We compared the simulation results (as described in the next section) with obser-
 145 vations from the Royal Netherlands Meteorological Institute (KNMI) observatory in Cabauw.
 146 Cabauw is located in the centre of the Netherlands (51.971 °N, 4.927 °E), where the sur-
 147 roundings are flat and mainly consist of meadows and ditches. At the measurement site,
 148 basic meteorological variables such as specific humidity, temperature and wind speed are
 149 measured at 7 levels along a 200 m high tower. Also, among others, there are measure-
 150 ments of the radiation budget components at the surface, surface fluxes, and cloud cover.
 151 These observations all have a 10 min resolution. We used these observations to validate
 152 the general performance of the LES model. For the main analyses, we used the observed
 153 shortwave irradiances (global, direct and diffuse) from the Baseline Surface Radiation
 154 Network (BSRN) site in Cabauw, which have a 1 sec resolution. Details about the mea-
 155 surements can be found in Knap (2018).

156 Apart from the observations, the clear sky radiation is available every minute, as
 157 calculated with the McClear model (Gschwind et al., 2019). The clear sky radiation is
 158 the amount of radiation that would have reached the surface if there were no clouds present.

159 3 Methods

160 3.1 Model Simulation

161 We performed realistic LESs using MicroHH (Van Heerwaarden et al., 2017). Our
 162 simulations use an interactive land-surface scheme, similar to HTESSSEL (Balsamo et al.,

2009) and our land surface is a homogeneous grassland. The 1D radiative transfer is calculated every 10 sec with RTE+RRTMGP (Pincus et al., 2019). We simulate realistic weather conditions by coupling our LES to ERA5 with a method similar to the one described by e.g. Neggers et al. (2012) and Schalkwijk et al. (2015). In short, in this setup, the atmosphere and soil are initialised from ERA5. Furthermore, the large scale forcings acting on the LES domain are reconstructed from ERA5 and added to the LES as time and height varying external forcings. These forcings are the advective tendencies of potential temperature, humidity and wind, the subsidence velocity, and geostrophic wind components. The domain mean state of the simulations is nudged towards ERA5 at a time scale of 3 hours, to prevent long experiments from drifting away from reality. For 4 July, the humidity close to the surface is much lower in ERA5 compared to the observations, thus we increased the initial humidity with 10% at the surface, and a linearly decreasing percentage above until roughly 1000 m (50 model levels). Additionally, we increased the nudging timescale to 12 h in the lowest 2 km (82 levels), to prevent the model from going towards the too dry ERA5 data.

Our domain has a size of 25.6 km x 25.6 km x 17 km, with a horizontal resolution of 50 m and a vertical grid spacing that increases with height, starting with 20 m grid spacing at the surface. Our LES uses double-periodic boundary conditions. We ran the simulations from 6 to 18 UTC (8-20 local time) and we saved the domain average statistics every 5 min. Additionally, we saved, every 10 sec, the results for an individual column in the centre of the domain ($x = y = 12.8$ km) and the horizontal cross sections for some key variables: liquid water path (including ice), shortwave downward radiation at the surface (both global and direct), cloud base height, cloud top height.

We investigated the probability distributions to compare the modeled radiation with the observations. We used the Probability Density Functions (PDFs) as used by Gristey et al. (2020). These PDFs show the relative occurrence of the radiation values. Therefore, they provide insight into the occurrence and strength of cloud shadows and cloud enhancements. Apart from changes in the cloud field, PDFs based on time series include the effect of the changing solar zenith angle (SZA). We correct for the changing SZA by dividing the radiation values of both the simulation and the observations by $\cos(\text{SZA})$ when PDFs are considered. Hereby, the radiation is normalised to a 0 degree solar zenith angle or, in other words, it is the radiation value as if the sun was right above the observer. For all PDFs, we used a binsize of 20 W m^{-2} and we resampled the observations to 10 sec averages, to match with the model resolution.

3.2 Smoothing Diffuse Radiation

We used a Gaussian filter to account for the 3D effects on diffuse radiation. This filter convolves the surface diffuse radiation from the 1D radiation model with a Gaussian distribution. This means that the diffuse radiation at one point becomes a weighted average of the point itself and its neighbours. In 1D, the weights are described by a Gaussian distribution (G_{1D}) of the form:

$$G_{1D}(x) = \frac{1}{\sqrt{2\pi}\sigma_{\text{filter}}} \exp\left(\frac{-x^2}{2\sigma_{\text{filter}}^2}\right).$$

In which σ_{filter} is the standard deviation of the distribution and x is the distance from the point of interest. The filter includes the neighbours within four times the standard deviation (σ_{filter}), so x ranges between $-4\sigma_{\text{filter}}$ and $+4\sigma_{\text{filter}}$. At the borders of the domain, the data is wrapped, meaning that data from the opposite side of the domain is included in the convolution. This is in line with the periodic boundaries of the simulations. To filter in 2D, 1D convolutions are performed in both horizontal directions subsequently. We tested the filtering for σ_{filter} between 0 and 1.5 km, in steps of 50 m, to

211 determine the optimal sigma (σ_{opt}). We determine σ_{opt} per time step. as we apply the
 212 Gaussian filter per time step.

213 3.3 Determining the Optimal Filter Size

214 We determine σ_{opt} by comparing the simulation with the observations. The sim-
 215 plest way to do this is to compare the standard deviation of the observations with the
 216 standard deviation of the simulated field. From the simulation, we used the standard de-
 217 viation of the diffuse radiation PDF after filtering (σ_{smooth}). This means that σ_{smooth}
 218 is calculated over a smoothed field normalised by $\cos(\text{SZA})$. Thus, σ_{smooth} is calculated
 219 per time step. The standard deviation of the observations (σ_{obs}) is calculated from the
 220 time series between 10 and 16 UTC, normalised by $\cos(\text{SZA})$. Therefore, σ_{obs} is con-
 221 stant. We consider the filtered distribution optimal if σ_{smooth} is as close as possible to
 222 σ_{obs} . The impact of using the standard deviation as the optimization criterion is discussed
 223 in section 5, as well as the impact of using σ_{obs} for all time steps.

224 3.4 Parameterization for the Filter Size

225 The optimal filter size (σ_{opt}) is a characteristic of the distribution of diffuse radi-
 226 ation, thus it is related to the cloud field. Therefore, σ_{filter} might be calculated as a func-
 227 tion of properties of this cloud field. A possible parameterization was proposed by Wissmeier
 228 et al. (2013). Their parameterization involves the calculation of σ_{filter} per grid cell per
 229 time step. We investigated the possibilities to have a parameterization with less differ-
 230 ent values of σ_{filter} by using one σ_{filter} per time step for the whole domain. We tested
 231 parameterizations of the simple form: $\sigma_{\text{filter}} = cv$, in which c is a constant and v a vari-
 232 able related to the cloud field. In section 5, we will discuss further how well one filter
 233 size can be used for the entire domain.

234 From existing literature, it is expected that σ_{filter} is related to the cloud base height
 235 and/or the solar zenith angle (Wissmeier et al., 2013; Wapler & Mayer, 2008). On top
 236 of that, we hypothesize that σ_{filter} is related to the sizes of the individual clouds, as the
 237 effect of small clouds can be filtered away with a narrow filter, whereas the effect of large
 238 clouds needs a wider filter to be filtered out. We used the maximum cloud size as a mea-
 239 sure for the cloud sizes present in the cloud field. The maximum cloud size is determined
 240 using a cloud tracking algorithm, as described by Heus and Seifert (2013). In short, all
 241 columns with a Liquid Water Path (LWP) larger than 5 g m^{-2} that are connected to each
 242 other are considered to form one cloud. The cloud size is than simply the square root
 243 of the area of the cloud. Apart from the maximum cloud size, we consider the cloud thick-
 244 ness and cloud cover for the parameterization of σ_{filter} as these variables are related to
 245 the maximum cloud size (Van Laar et al., 2019). It should be noted that cloud cover,
 246 mean cloud base height, and mean cloud thickness are calculated directly from the LES
 247 output, so all columns containing any liquid water are included here. The cloud sizes are
 248 derived from the cloud tracking, hence they only include columns with an LWP larger
 249 than 5 g m^{-2} . In summary, we considered cloud thickness, cloud cover, cloud base height,
 250 solar zenith angle, and maximum cloud size to determine the best parameterization for
 251 σ_{filter} .

252 4 Results

253 We will first show the general development of the simulations and compare it to
 254 the observations. Then, we will discuss the distribution of the radiation in detail, fol-
 255 lowed by the filtering of the radiation and the possible parameterizations for this filter.

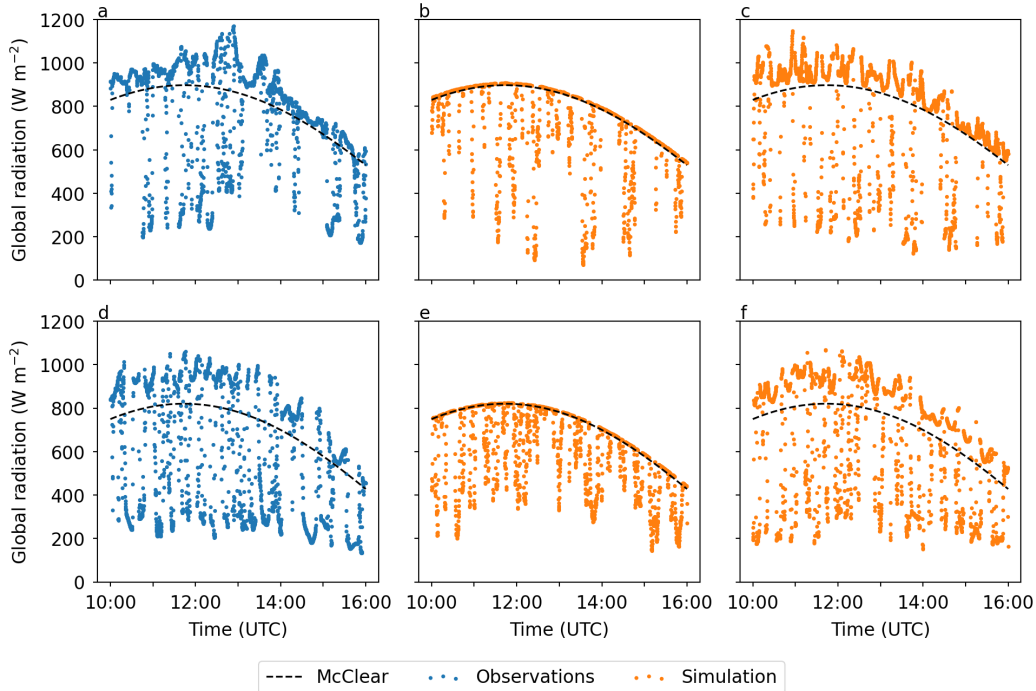


Figure 1. Timeseries of global radiation as (a) observed, (b) simulated and (c) filtered for 4 July. (d), (e) and (f) are as (a), (b) and (c), but for 15 August. For the simulations, the time series are taken at the centre point of the domain.

256

4.1 Case Description and Model Validation

257

258

259

260

261

262

263

264

The timeseries of observed global radiation (Fig. 1a, d) show that the global radiation is either higher or lower than under clear sky conditions. The global radiation is lower than the clear sky value in a cloud shadow. When there is no cloud shadow, the radiation is enhanced by diffuse radiation scattered by a nearby cloud. In the simulation with 1D radiative transfer (Fig. 1b, e), the global radiation is either lower than or equal to the radiation under clear-sky conditions, meaning that cloud shadows occur, but cloud enhancements are not simulated. The rightmost panels in Fig. 1 show the time-series after we filtered the diffuse radiation. These will be discussed in section 4.3.

265

266

267

268

269

270

271

Fig. 2 shows the timeseries of cloud cover, temperature and humidity. Comparing the model simulations with the observations shows that the simulations accurately capture realistic weather conditions. The simulation results are more smooth, because they are average values over the model domain, whereas the observations are at one location. For 4 July, the simulated cloud onset is a bit later than in the observations, whereas for 15 August it is a bit earlier. In general, although the modelled cloud structures will never be exactly as observed, the cloud cover is well simulated.

272

273

274

275

276

277

278

The simulated vertical profiles (Fig. 3) show that, in both cases, a stable boundary layer was present at the beginning of the day, at 6 UTC. The addition of sensible heat caused the boundary layer to grow and heat up. In the afternoon, the boundary layer was well mixed. On 4 July, the humidity above the boundary layer increases over time, but the changes are only small close to the boundary layer top. In general, only small changes in the profiles occur above the boundary layer, indicating that large scale advection plays a minor role. On both days, the local surface fluxes determine the de-

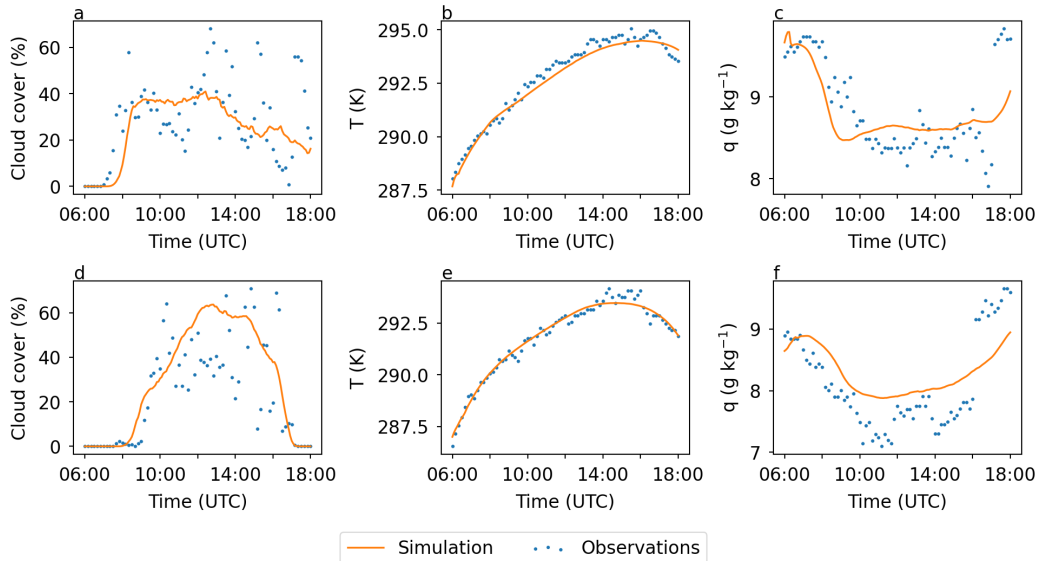


Figure 2. Time series of (a) cloud cover, (b) temperature and (c) specific humidity for 4 July. (d), (e) and (f) are as (a), (b) and (c), but for 15 August. Temperature and humidity are at 10m height.

279 velopment of the profiles during the day, which makes these days suitable case studies.
 280 The profiles of liquid water show that clouds are formed under the inversion (Fig. 3c,
 281 f). On the 15th of August, a strong inversion was present at the top of the boundary layer
 282 (Fig. 3d, e). The clouds spread out horizontally under the inversion, as the inversion pre-
 283 vents the clouds from growing in the vertical. This causes relatively thin clouds and a
 284 high cloud cover (Fig. 2d) for a case with shallow cumulus clouds. The clouds on both
 285 days clearly differ in their thickness and liquid water content. Thus, we can get an in-
 286 dication of how well our method works for different cumulus conditions, by testing our
 287 filtering method for these two days. In the remainder of this paper, we will focus on the
 288 hours between 10 UTC and 16 UTC when clouds are observed and simulated on both
 289 days.

290 4.2 1D Radiative Transfer

291 In this section, we examine the surface irradiance from the simulation with 1D ra-
 292 diation by looking at PDFs of global, direct and diffuse radiation (Fig. 4) and an exam-
 293 ple of the surface radiation fields in the simulation (Fig. 5, top row). We will first dis-
 294 cuss the differences between the observations and the simulation with 1D radiation. The
 295 PDFs and surface fields of the simulation after filtering will be discussed in the next sec-
 296 tion.

297 The simulated distribution of global radiation does not resemble the observed dis-
 298 tribution (Fig. 4a, d). This is in line with the results of Gristey et al. (2020) and Schmidt
 299 et al. (2007). The differences between the observations and the simulation can be explained
 300 by considering the direct and diffuse radiation separately (Fig. 4) and from the spatial
 301 patterns (Fig. 5, top row).

302 The direct radiation is low in the cloud shadows and high in other areas. The sim-
 303 ulated diffuse radiation is high under the clouds (Fig. 5b). This partly compensates for
 304 the reduced direct radiation. Under the clouds, the diffuse radiation is highest in areas

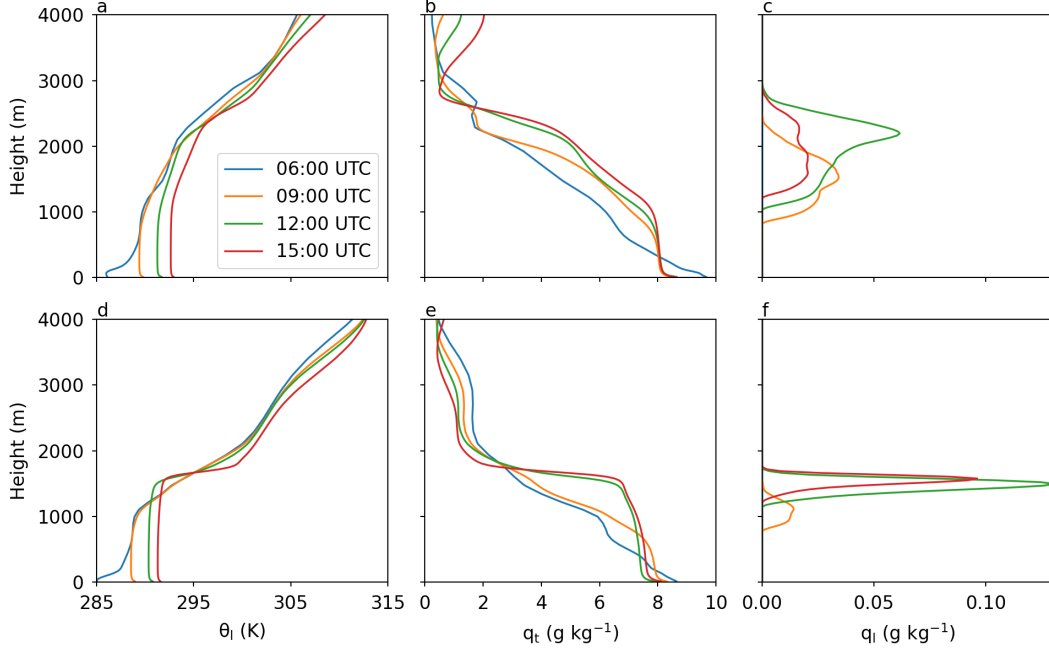


Figure 3. Domain-average vertical profiles of (a) liquid water potential temperature, (b) specific humidity, (c) liquid water specific humidity for 4 July. (d), (e) and (f) are as (a), (b) and (c), but for 15 August.

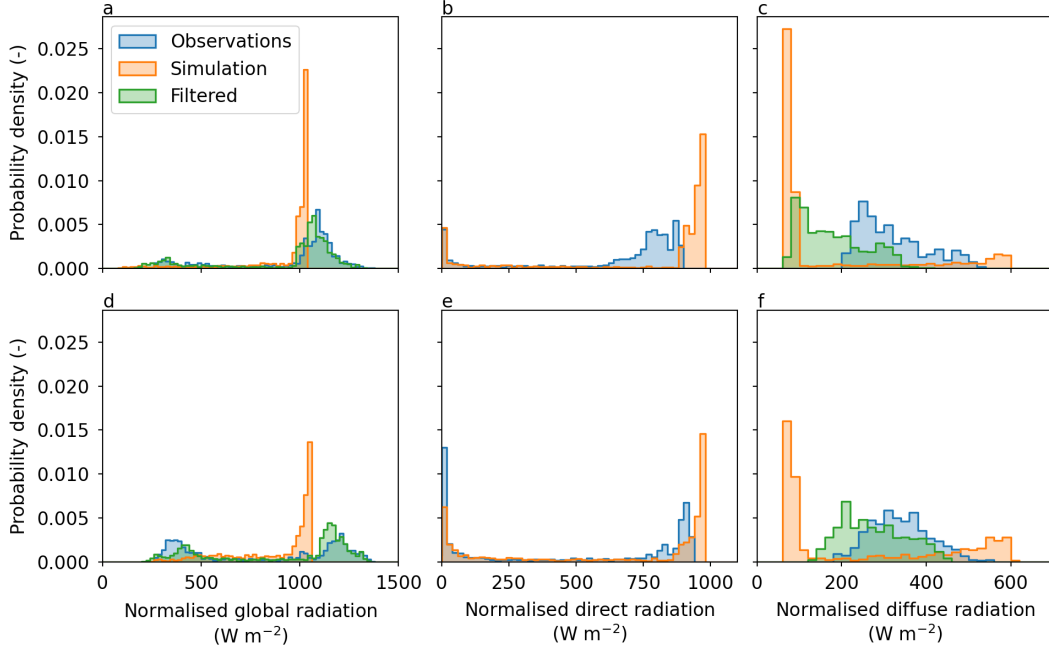


Figure 4. PDFs of (a) global radiation, (b) direct radiation, (c) diffuse radiation for the observations, the original simulation and the simulation after filtering for 4 July. (d), (e) and (f) are as (a), (b) and (c), but for 15 August. For these PDF, the time series from 10 to 16 UTC are used. For the simulation, the time series is taken at the centre point of the domain. All values are normalised by $\cos(\text{SZA})$.

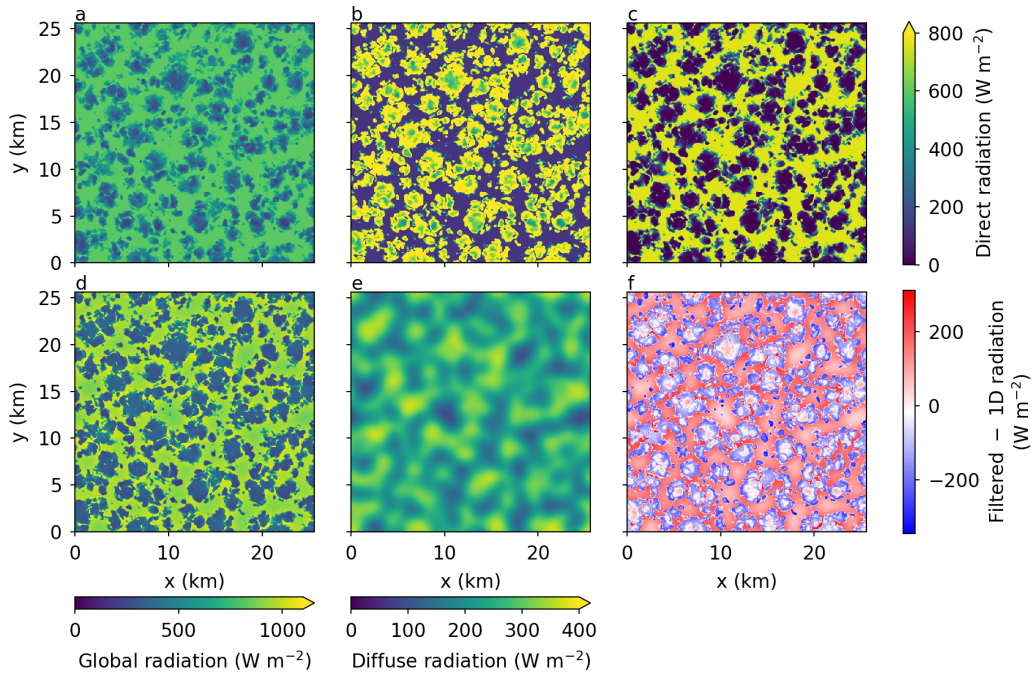


Figure 5. Surface fields at 15 August 12 UTC. The first row shows the original fields of (a) global radiation, (b) diffuse radiation, and (c) direct radiation. The second row shows the fields after filtering the diffuse radiation of (d) global radiation and (e) diffuse radiation. (f) shows the difference in radiation between the original and filtered simulation. Note that we did not change the direct radiation. Therefore, the difference in (f) is the difference in diffuse radiation (b vs e) as well as the difference in global radiation (a vs d). The SZA is 37.9° .

305 with a low LWP. In areas with a high LWP, the diffuse radiation is reduced as more ra-
 306 diation is absorbed. In simulations with 1D radiation, the cloud shadows are located ex-
 307 actly below the clouds (Fig. 5c). From simple geometry, it is clear that the shadow of
 308 a cloud is not directly below a cloud, unless the sun is right above the cloud. Addition-
 309 ally, the cloud shadows are too small in simulations with 1D radiation, as only the top
 310 of the cloud intercepts radiation. In reality, the radiation falls on the cloud under an an-
 311 gle, thus part of the cloud sides also intercepts radiation, causing a larger cloud shadow.
 312 Previous studies showed that the, more complex, Tilted Independent Column Approx-
 313 imation (TICA) can be used to simulate the cloud shadows correctly in terms of both
 314 size and location (Wapler & Mayer, 2008; Várnai & Davies, 1999).

315 The spatial radiation patterns result in the PDFs shown in Fig. 4. The PDFs of
 316 the direct radiation show peaks at the high and low end of the distribution, for both ob-
 317 servations and simulations (Fig. 4b, e). The high values of simulated direct radiation are
 318 higher than the maximum observed direct radiation. In line with this overestimation,
 319 the average diffuse radiation is underestimated (Fig. 4c, f). This is also observed for the
 320 clear sky radiation, indicating that the difference might be the effect of aerosols, which
 321 are not included in the radiation calculations. The impact hereof is discussed in section
 322 5. The simulated diffuse radiation PDF is dominated by the low amounts of diffuse ra-
 323 diation under clear sky conditions. This is clearly not in line with the observed PDF (Fig.
 324 4c, f). Thus, we find that the differences in the smoothness of the global radiation field
 325 and thereby the shape of the global radiation PDF are primarily caused by differences
 326 in the diffuse radiation, which is in line with the findings of Gristey et al. (2020). Hence,
 327 to correctly represent the variability of the radiation, i.e. to get the PDF correct, it is
 328 essential to correct for the horizontal transport of diffuse radiation, but it is not neces-
 329 sary to correct the direct radiation.

330 4.3 Smoothing Diffuse Radiation

331 We applied a spatial filter, to account for the horizontal spreading of diffuse radi-
 332 ation. Then, we combined the filtered diffuse radiation with the original direct radiation,
 333 to obtain the new global radiation. This means that we introduced the horizontal spread-
 334 ing of the diffuse radiation, but not the 3D effect on the direct radiation. Fig. 5d, e shows
 335 an example of the resulting surface radiation fields. The difference between the original
 336 and filtered fields is shown in Fig. 5f. The difference in Fig. 5f is the difference in dif-
 337 fuse radiation as well as the difference in global radiation, as we did not change the di-
 338 rect radiation. The difference plot makes clear how the filtering influences the radiation.
 339 Diffuse radiation is reduced in the regions where it was originally the highest, thus un-
 340 der the clouds. Diffuse radiation is increased in the regions where it was originally low,
 341 thus in the clear sky patches and in the centres of the clouds. The cross section of dif-
 342 fuse radiation at the surface (Fig. 5e) shows that the highest amounts of diffuse radi-
 343 ation still occur below the clouds, but the areas around the clouds also receive diffuse
 344 radiation. This is in line with results from 3D simulations (Gristey et al., 2020). Fur-
 345 thermore, it is in line with the results of Wissmeier et al. (2013), who showed that fil-
 346 tering the diffuse radiation can greatly improve the surface radiation fields. Combining
 347 the filtered diffuse radiation field (Fig. 5e) with the original direct radiation field (Fig.
 348 5c) results in the global radiation field shown in Fig. 5d. This global radiation field shows
 349 cloud enhancements in addition to the cloud shadows and clear sky patches.

350 The impact of the filtering is also clearly visible in the PDFs (Fig. 4) and time-
 351 series (Fig. 1c, f). The shape of the simulated diffuse radiation PDFs closely matches
 352 the shape of the observed PDF, when the diffuse radiation is filtered with the optimal
 353 filter width (σ_{opt}). The PDFs of global radiation are now bimodal. There is one peak
 354 at the low irradiance values, showing that the cloud shadows became darker. The sec-
 355 ond peak is at higher irradiance values than the original peak, showing that the irradi-
 356 ance in regions other than the cloud shadows is increased. These cloud enhancements are

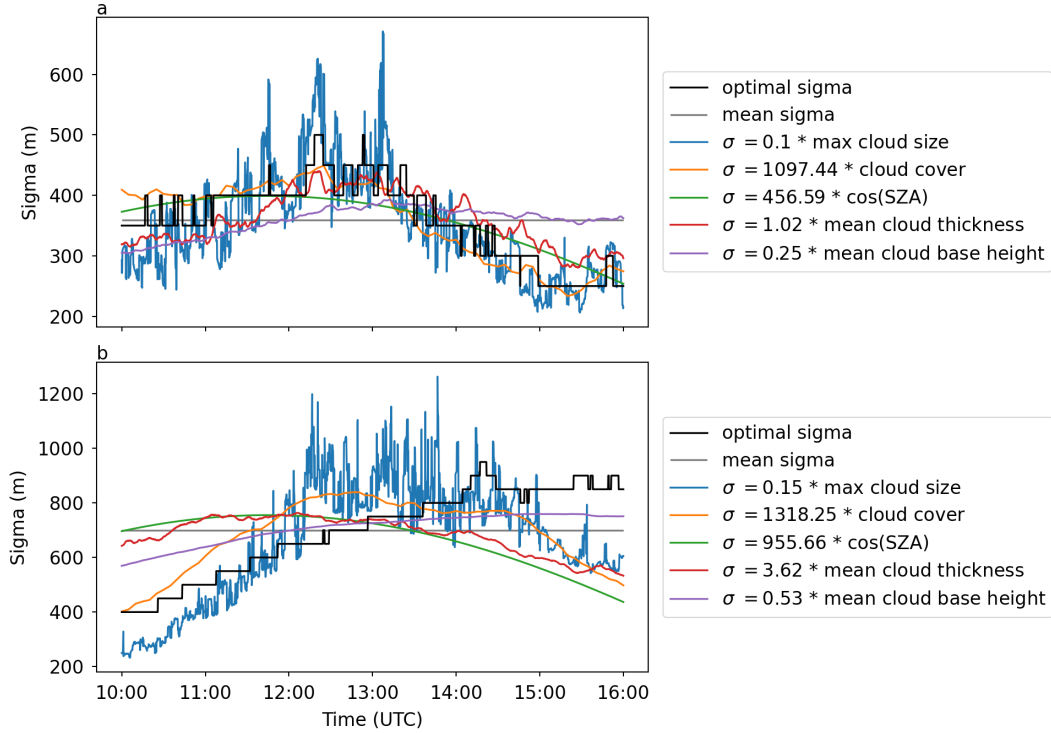


Figure 6. Time series of σ_{filter} for (a) 4 July and (b) 15 August (b). σ_{opt} , the mean of σ_{opt} and σ_{filter} as a linear function of the maximum cloud size, the cloud cover, the cosine of the solar zenith angle, the mean cloud thickness and mean cloud base height.

357 also clearly visible in the timeseries. Before filtering, the McClear value was simulated
 358 in the clear sky periods. After filtering, the cloud enhancements are simulated and their
 359 magnitude is in line with the peaks in the observations. Furthermore, before filtering,
 360 some cloud shadows were much darker than others. After filtering, the cloud shadows
 361 are more similar, which is also in line with the observations. Together, Fig. 4 and Fig.
 362 1 show that our filtering method greatly improves the model results.

363 4.4 Sigma Parameterization

364 Next, we want to parameterize σ_{filter} as a function of the cloud properties in the
 365 simulation, to be able to filter the diffuse radiation in a simulation. Therefore, we inves-
 366 tigated how well σ_{opt} can be described as a function of cloud thickness, cloud cover, cloud
 367 base height, solar zenith angle, and maximum cloud size. The time series of σ_{opt} are shown
 368 in Fig. 6. Note that for 15 August, the range of σ shown is larger than for 4 July. On
 369 the 15th of August, σ_{opt} increases during most of the period and is fairly constant at the
 370 end. On the 4th of July, σ_{opt} increases a bit in the first three hours and decreases after-
 371 wards. The average σ_{opt} on 15 August is 700 m, which is close to the 625 m found by
 372 Wissmeier et al. (2013) for their case with cumulus mediocris. For 4 July, we find a smaller
 373 average σ_{opt} of 360 m.

374 The optimal filter size (σ_{opt}) can be parameterized by relating it to the cloud field.
 375 Fig. 6 shows simple approximations of σ_{opt} . The maximum cloud size, cloud cover, $\cos(\text{SZA})$
 376 and mean cloud thickness all show an increase in the beginning of the period and a de-
 377 crease later on. For 4 July, this is exactly what we also observe for σ_{opt} . For 15 August,
 378 we do not find a decrease in σ_{opt} at the end of the period, which is best captured by the

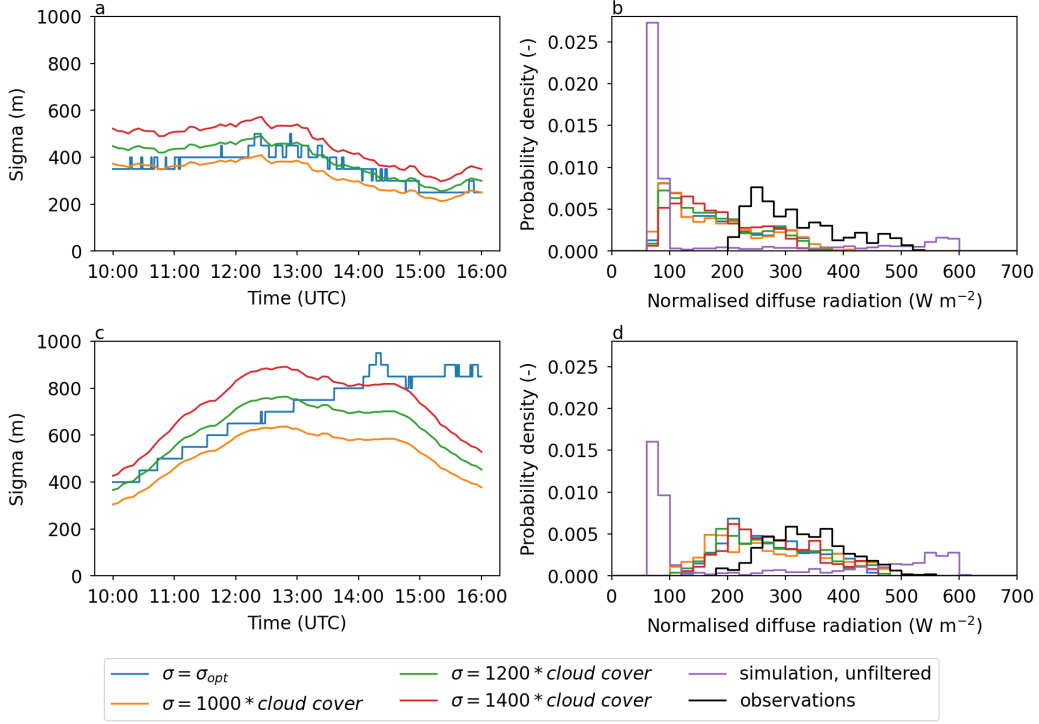


Figure 7. (a) timeseries of σ_{opt} and approximations of σ_{filter} as a function of the cloud cover. (b) PDFs of the diffuse radiation for the observations, original 1D simulation and filtered simulation. For these PDF, the time series from 10 to 16 UTC are used. For the simulation, the time series is taken at the centre point of the domain. All values are normalised by $\cos(SZA)$. For the filtering, the σ 's from (a) are used. (c) and (d) are as (a) and (b), but for 15 August.

379 approximation based on the cloud base height. This shows that it is not straightforward
 380 to relate σ_{filter} to the cloud properties. To fully understand the development of σ_{opt} one
 381 would need to consider multiple variables and (possibly) non-linear relationships. How-
 382 ever, Fig. 6 also shows that with a linear function of one variable, we can reasonably ap-
 383 proximate σ_{opt} for both days.

384 The constants that we find to relate the cloud variables to σ_{opt} differ quite a bit
 385 between the days. For the $\cos(SZA)$, mean thickness and mean cloud base height, the
 386 constant is more than twice as large for 15 August, compared to 4 July. For the cloud
 387 cover and maximum cloud size, the constants differ less, and are around 1100-1300 for
 388 the cloud cover and 0.1-0.15 for the maximum cloud size. This indicates that the max-
 389 imum cloud size and cloud cover can potentially be used for a parameterization of σ_{opt} .
 390 The advantage of the cloud cover is that it is readily available in the model, whereas the
 391 maximum cloud size has to be obtained with a cloud tracking algorithm (Heus & Seifert,
 392 2013). We further explore the possibilities to use the cloud cover to approximate σ_{opt}
 393 in the next section.

394 4.5 Sigma Sensitivity

395 It is important to know how sensitive the resulting PDFs are to a change in σ_{filter} ,
 396 as σ_{filter} differs depending on which parameterization is used. We defined three possi-
 397 ble approximations of σ_{opt} as a function of the cloud cover, with the constant being 1000,

1200 and 1400 (Fig. 7a, c). For most of the times, all three approximations are close to σ_{opt} . Only for the last hour at 15 Augustus, the parameterizations deviate strongly from σ_{opt} . Fig. 7b and d show the PDFs of diffuse radiation that are obtained when using the different approximations of σ_{filter} . The differences between the three possible approximations are small, as well as the differences between the approximations and σ_{opt} . This shows that with a rough approximation of σ_{filter} we can reach a clear improvement, compared to the original 1D radiative transfer calculations.

5 Discussion

In this section, we reflect on the assumptions made while comparing the observations to the simulations.

First, we assumed that one value for σ_{obs} is representative for the hours between 10 and 16 UTC. Calculating σ_{obs} over different, shorter periods results in different values for σ_{obs} , which would have resulted in different values for σ_{opt} . Ideally, the time-span over which σ_{obs} is calculated is related to the changes in the cloud field. If the cloud field changes, the standard deviation should change accordingly. However, the averaging period should also be long enough to have a statistically reasonable estimate for σ_{obs} . Furthermore, σ_{obs} depends on the clouds that pass over the sensor and the size of these clouds in the direction of the wind. A better representation of the cloud field in all directions can be obtained by performing measurements in a grid. Gristey et al. (2020) used observations from 10 locations to study the relation between the cloud fraction and the cloud radiative effect. Their results indicate that the observation density should be at least one order of magnitude larger to be able to detect the relationships found in model simulations. Alternatively, one could base σ_{opt} on a 3D simulation instead of observations, as was done before by e.g. Wissmeier et al. (2013) and Zuidema and Evans (1998).

Second, we assumed that σ_{filter} is optimal if the resulting standard deviation is as close as possible to the standard deviation of the observations. A matching standard deviation does not guarantee that the PDFs also have a similar shape. To determine the impact hereof, we determined σ_{opt} also from the shapes of the PDFs. To this end, we described the shape of the observed PDF by fitting a gamma distribution through it. Then, we determined σ_{opt} by minimizing the Euclidean distance between the filtered PDF and the fitted gamma-distribution. There was no clear improvement in the PDFs, although the obtained σ_{opt} based on the shape is in general a bit larger. We therefore argue that the simple matching of the standard deviations functions well enough.

Third, a matching standard deviation also does not guarantee that the PDFs have a similar mean. From Fig. 4c, f, it became clear that the diffuse radiation is on average too low in our simulations. This underestimation has two causes. The modelled and observed clouds might be slightly different. Although the cloud cover is similar in the observations and simulations, the cloud structures might be different. We also find an underestimation of the clear-sky diffuse radiation, which cannot be related to differences in the cloud field. This underestimation is likely caused by the lack of aerosols in the model simulation. The underestimation is larger on 4 July (maximum 70 W m^{-2}) than on 15 August (maximum 50 W m^{-2}), which is in line with the larger aerosol optical depth on 4 July compared to 15 August. (We compared the aerosol optical depths from the McClear model (Gschwind et al., 2019), not shown.) We assume that the aerosols mainly influence the average amount of diffuse radiation and that they have a limited impact on the shape of the PDF. Under clear-sky conditions, the impact of aerosols is homogeneous, thus aerosols only impact the average amount of diffuse radiation and not the shape of the PDF. For broken cloud conditions, Schmidt et al. (2009) showed that aerosols reduce the irradiance in the gaps between the clouds, by scattering radiation to the cloudy regions. Thus, the PDFs of the global radiation are influenced by the presence of aerosols (Schmidt et al., 2009). Aerosols do not only scatter radiation (direct effect of aerosols),

449 but aerosols also interact with nearby clouds (indirect effect of aerosols). The relative
 450 importance of these effects is uncertain as it depends on characteristics of both the clouds
 451 and the aerosols (Boucher et al., 2013). The difference between the PDFs with and with-
 452 out aerosols (Schmidt et al., 2009) is small compared to the difference between a 1D and
 453 3D simulation (Fig. 4a, d). We can therefore assume that the impact of the aerosols on
 454 the shape of the PDF is minor compared to the impact of the 3D effects of the clouds.

455 Fourth, we assumed that one σ_{filter} can be used for the whole domain. On the two
 456 selected days, the cloud properties were homogeneous in space over an area larger than
 457 our domain size. For these cases, our results show that we can greatly improve the ra-
 458 diation field with one filter size. Thus, one σ_{filter} is applicable to a cloud field, in which
 459 clouds properties are homogeneous in space. It might be insufficient to use one filter size
 460 when the domain is larger and/or the cloud properties are not statistically the same in
 461 the whole domain. However, there is no need to calculate a filter size per grid cell as done
 462 by Wissmeier et al. (2013), as we showed that one filter size can be used for a cloud field.

463 Lastly, the specific conditions of the selected cases impacted our current results.
 464 From the work of Wissmeier et al. (2013) it is clear that filtering can be applied success-
 465 fully to a wide range of cases. Therefore, we expect that filtering with one σ_{filter} will be
 466 applicable to a wide range of cases as well.

467 6 Conclusion

468 In this work, we described a simple approach to correct the unrealistic surface solar
 469 irradiance fields that arise from LES with 1D radiative transfer. Horizontal trans-
 470 fer of radiation is omitted in 1D, resulting in a misplacement of the cloud shadows and
 471 a lack of horizontal spreading of diffuse radiation. We approximated the horizontal spread-
 472 ing of the diffuse radiation by filtering the diffuse radiation at the surface with a Gaus-
 473 sian filter. Filtering the diffuse radiation resulted in a PDF of global radiation that closely
 474 matches the observations. The time series of global radiation after filtering show the char-
 475 acteristic cloud enhancements that were not simulated with the 1D radiation model. The
 476 width of our filter can be approximated with a linear function of only one cloud variable,
 477 e.g. the cloud cover. Furthermore, we showed that small deviations from the optimal fil-
 478 ter width do not change the resulting PDF much. Our results suggest that our method
 479 could be further improved by including aerosols, especially on days with a high aerosol
 480 optical depth, as this should reduce the overestimation of direct radiation and accom-
 481 panying underestimation of diffuse radiation. The results show that the used approach
 482 has the potential to correct for the 3D radiative effect by adding minimal changes to ex-
 483 isting methods. This assures that the impact on computational times is small. First tests
 484 showed that the filtering increases the total runtime of the model with less than 1%. There-
 485 fore, this method has the potential to be applied to many more days and different lo-
 486 cations in the future. The implementation of the diffuse radiation filtering will assure
 487 a more realistic representation of the surface irradiance. This directly improves model
 488 results regarding the surface, for example when studying the impact of radiation on re-
 489 newable energy production by solar panels or the impact on surface processes such as
 490 photosynthesis. Additionally, the improved representation of the surface irradiance can
 491 contribute to a better representation of the surface fluxes and with that a better repre-
 492 sentation of the cloud dynamics.

493 7 Open Research

494 All data and scripts used to conduct this research are added for peer review in the
 495 folder data&scripts.zip. This information will be made available in a repository once the
 496 manuscript is accepted.

Acknowledgments

We acknowledge funding from the Wageningen Institute for Environment and Climate Research (WIMEK) and the Dutch Research Council (NWO) (grant: VI.Vidi.192.068). The simulations are carried out on the Dutch national e-infrastructure with the support of SURF Cooperative.

References

- Balsamo, G., Beljaars, A., Scipal, K., Viterbo, P., van den Hurk, B., Hirschi, M., & Betts, A. K. (2009). A revised hydrology for the ECMWF model: Verification from field site to terrestrial water storage and impact in the Integrated Forecast System. *Journal of hydrometeorology*, *10*(3), 623–643.
- Boucher, O., Randall, D., Artaxo, P., Bretherton, C., Feingold, G., Forster, P., . . . Zhang, X. (2013). Clouds and aerosols. In *Climate change 2013: the physical science basis. Contribution of Working Group I to the Fifth Assessment Report of the Intergovernmental Panel on Climate Change* (pp. 571–657). Cambridge University Press.
- Gristey, J., Feingold, G., Glenn, I., Schmidt, K., & Chen, H. (2020). Surface solar irradiance in continental shallow cumulus fields: Observations and large-eddy simulation. *Journal of the Atmospheric Sciences*, *77*(3), 1065–1080.
- Gronemeier, T., Kanani-Sühring, F., & Raasch, S. (2017). Do shallow cumulus clouds have the potential to trigger secondary circulations via shading? *Boundary-Layer Meteorology*, *162*(1), 143–169.
- Gschwind, B., Wald, L., Blanc, P., Lefèvre, M., Schroedter-Homscheidt, M., & Arola, A. (2019). Improving the McClear model estimating the downwelling solar radiation at ground level in cloud-free conditions – McClear-v3. *Meteorologische Zeitschrift*, *28*(2), 147–163.
- Heus, T., & Seifert, A. (2013). Automated tracking of shallow cumulus clouds in large domain, long duration large eddy simulations. *Geoscientific Model Development*, *6*(4), 1261.
- Hogan, R., Schäfer, S. A., Klinger, C., Chiu, J. C., & Mayer, B. (2016). Representing 3-D cloud radiation effects in two-stream schemes: 2. Matrix formulation and broadband evaluation. *Journal of Geophysical Research: Atmospheres*, *121*(14), 8583–8599.
- Hogan, R., & Shonk, J. (2013). Incorporating the effects of 3D radiative transfer in the presence of clouds into two-stream multilayer radiation schemes. *Journal of the atmospheric sciences*, *70*(2), 708–724.
- Jakub, F., & Mayer, B. (2015). A three-dimensional parallel radiative transfer model for atmospheric heating rates for use in cloud resolving models—The Ten-Stream solver. *Journal of Quantitative Spectroscopy and Radiative Transfer*, *163*, 63–71.
- Jakub, F., & Mayer, B. (2017). The role of 1-D and 3-D radiative heating in the organization of shallow cumulus convection and the formation of cloud streets. *Atmospheric Chemistry and Physics*(21), 13317–13327.
- Kanniah, K., Beringer, J., North, P., & Hutley, L. (2012). Control of atmospheric particles on diffuse radiation and terrestrial plant productivity: A review. *Progress in Physical Geography*, *36*(2), 209–237.
- Knap, W. (2018). *Basic and other measurements of radiation at station Cabauw (2018-08)* [data set]. PANGAEA. Retrieved from <https://doi.org/10.1594/PANGAEA.893843> doi: 10.1594/PANGAEA.893843
- Kreuwel, F., Knap, W., Visser, L., van Sark, W., Vilà-Guerau de Arellano, J., & van Heerwaarden, C. (2020). Analysis of high frequency photovoltaic solar energy fluctuations. *Solar Energy*, *206*, 381–389.
- Marshak, A., Davis, A., Wiscombe, W., & Cahalan, R. (1995). Radiative smoothing in fractal clouds. *Journal of Geophysical Research: Atmospheres*, *100*(D12),

- 550 26247–26261.
- 551 Mayer, B. (2009). Radiative transfer in the cloudy atmosphere. In *Epj web of confer-*
 552 *ences* (Vol. 1, pp. 75–99).
- 553 Neggers, R. A., Siebesma, A., & Heus, T. (2012). Continuous single-column model
 554 evaluation at a permanent meteorological supersite. *Bulletin of the American*
 555 *Meteorological Society*, *93*(9), 1389–1400.
- 556 Pincus, R., Mlawer, E., & Delamere, J. (2019). Balancing accuracy, efficiency, and
 557 flexibility in radiation calculations for dynamical models. *Journal of advances*
 558 *in modeling earth systems*, *11*(10), 3074–3089.
- 559 Schäfer, S. A., Hogan, R. J., Klinger, C., Chiu, J. C., & Mayer, B. (2016). Repre-
 560 senting 3-D cloud radiation effects in two-stream schemes: 1. Longwave con-
 561 siderations and effective cloud edge length. *Journal of Geophysical Research:*
 562 *Atmospheres*, *121*(14), 8567–8582.
- 563 Schalkwijk, J., Jonker, H. J., Siebesma, A. P., & Bosveld, F. C. (2015). A year-
 564 long large-eddy simulation of the weather over cabauw: An overview. *Monthly*
 565 *Weather Review*, *143*(3), 828–844.
- 566 Schmidt, K., Feingold, G., Pilewskie, P., Jiang, H., Coddington, O., & Wendisch,
 567 M. (2009). Irradiance in polluted cumulus fields: Measured and modeled
 568 cloud-aerosol effects. *Geophysical research letters*, *36*(7).
- 569 Schmidt, K., Venema, V., Giuseppe, F. D., Scheirer, R., Wendisch, M., & Pilewskie,
 570 P. (2007). Reproducing cloud microphysical and irradiance measurements
 571 using three 3D cloud generators. *Quarterly Journal of the Royal Meteorolog-*
 572 *ical Society: A journal of the atmospheric sciences, applied meteorology and*
 573 *physical oceanography*, *133*(624), 765–780.
- 574 Van Heerwaarden, C., van Stratum, B., Heus, T., Gibbs, J., Fedorovich, E., & Mel-
 575 lado, J. (2017). MicroHH 1.0: a computational fluid dynamics code for direct
 576 numerical simulation and large-eddy simulation of atmospheric boundary layer
 577 flows. *Geoscientific Model Development*, *10*, 3145–3165.
- 578 Van Laar, T., Schemann, V., & Neggers, R. (2019). Investigating the diurnal evo-
 579 lution of the cloud size distribution of continental cumulus convection using
 580 multiday les. *Journal of the Atmospheric Sciences*, *76*(3), 729–747.
- 581 Várnai, T., & Davies, R. (1999). Effects of cloud heterogeneities on shortwave radi-
 582 ation: Comparison of cloud-top variability and internal heterogeneity. *Journal*
 583 *of the atmospheric sciences*, *56*(24), 4206–4224.
- 584 Veerman, M., Pedruzo-Bagazgoitia, X., Jakub, F., Vilà-Guerau de Arellano, J., &
 585 van Heerwaarden, C. (2020). Three-dimensional radiative effects by shallow
 586 cumulus clouds on dynamic heterogeneities over a vegetated surface. *Journal*
 587 *of Advances in Modeling Earth Systems*, *12*(7).
- 588 Wapler, K., & Mayer, B. (2008). A fast three-dimensional approximation for the cal-
 589 culation of surface irradiance in large-eddy simulation models. *Journal of Ap-*
 590 *plied Meteorology and Climatology*, *47*(12), 3061–3071.
- 591 Wissmeier, U., Buras, R., & Mayer, B. (2013). paNTICA: A fast 3D radiative
 592 transfer scheme to calculate surface solar irradiance for NWP and LES models.
 593 *Journal of applied meteorology and climatology*, *52*(8), 1698–1715.
- 594 Zuidema, P., & Evans, K. (1998). On the validity of the independent pixel approx-
 595 imation for boundary layer clouds observed during ASTEX. *Journal of Geo-*
 596 *physical Research: Atmospheres*, *103*(D6), 6059–6074.